

# Orbital Angular Momentum of photons: a tool to transmit information

João Sabino

MEFT, *Departamento de Física, Instituto Superior Técnico, Av. Rovisco Pais, 1049-001 Lisboa, Portugal*

September 2016

## Abstract

Communication systems have seen a great evolution in the second half of last century, allowing faster and better communications all over the world. In particular, optical communications have become the back bone of high capacity wired communications. The internet data traffic capacity is rapidly reaching the limits imposed by optical fiber non-linear effects. Orbital Angular Momentum (OAM) of light is a potential solution that permits the generation of many orthogonal modes which adds another degree of freedom to carry information. In this work simulations are developed as a model to the propagation and diffraction of OAM-carrying beams and a proof-of-concept information transmission using OAM is also implemented, showing that this property of light can be used to increase the spectral efficiency of today's networks.

## 1 Introduction

The existence of our society as we know it nowadays would not have been possible without the development in communication systems. In the second half of the last century, the progress on telecommunication systems made it possible to communicate almost instantly with any part of the world [1]. This development is due to the transition from analog to digital systems which brought the ability to transmit data with fundamentally no loss of quality [2]. Moreover, the breakthroughs in semiconductor technologies enabled the processing of all kinds of information, through cheap and power efficient micro-chips [3].

At the same time, the need for data transmission brought new technological challenges, because transportation of data was (and still is) demanded at all scales, from short on-chip buses [4] to long-haul networks all across the world[5]. These challenges were overcome using electronic, radio-frequency or optical communication systems.

Whenever high aggregate bit rates or long transmissions are needed, optical communication sys-

tems are preferable for two main reasons: first, the high optical carrier frequencies allow for high-capacity systems at small relative bandwidths; second, transmission losses at optical frequencies are usually very small compared to baseband electronic or radio-frequency technologies (today's optical telecommunication fibers exhibit losses of 0.2 dB/km, one or two orders of magnitude lower compared to other technologies) [6].

Since the flux of information has been increasing, one of the goals of optical communications community is to achieve higher data transmission capacity. This has led to investigation of different physical properties of light such as amplitude, phase, wavelength, polarization to encode information. Spatially orthogonal modes and spatial position have also been investigated, since multiplexing of different data channels is a common way of increasing data transmission capacity. OAM is a property of light that has been under intensive research. It is a discrete property and can be interpreted to characterize the "twist" of a helical phasefront. OAM has shown to be worth studying since beams with different "twist" are orthogonal when propagating

coaxially, making it useful in the improvement of optical communications performance [7]. To better understand this light property, we may start by saying that it is known from Maxwell's theory that electromagnetic radiation carries energy and momentum [8]. Further investigations [9] proved that light also carries angular momentum, which is divided in two parts: a spin part and an orbital part [8]. The spin part is associated with polarization and we know that for a single photon it may take the values  $\pm\hbar$  for right-handed and left-handed circular polarization [10]; the orbital part is associated to spatial distribution and its values are known to be  $l\hbar$  per photon, where  $l$  is an integer. The following calculations should clarify the statements above.

To study the OAM of an electromagnetic wave, we should find a solution for the Helmholtz equation that allows the existence of angular momentum on the  $z$  direction [11]. The Laguerre Gaussian (LG) beams are a solution of Helmholtz equation in cylindrical coordinates  $r, \phi, z$  and are described, in the paraxial approximation [8], by equation 1,

$$\begin{aligned}
u_{pl}(r, \phi, z) = & \frac{C}{(1 + z^2/z_R^2)^{1/2}} \left( \frac{r\sqrt{2}}{w(z)} \right) L_p^l \left( \frac{2r^2}{w^2(z)} \right) \\
& \times \exp \left( i(2p + l + 1) \tan^{-1} \left( \frac{z}{z_R} \right) \right) \\
& \times \exp \left( \frac{-r^2}{w^2(z)} \right) \exp \left( \frac{-ikr^2z}{2(z^2 + z_R^2)} \right) \\
& \times \exp(ikz) \exp(-il\phi).
\end{aligned} \tag{1}$$

where  $z_R$  is the Rayleigh range,  $w$  is the waist of the beam,  $k$  is the wave number,  $p + 1$  is the number of intensity annular regions,  $l$  is the azimuthal mode index, also called topological charge, and  $C$  is a normalization constant. As shown in figure 1, these beams have  $l$  helical wave fronts and have an azimuthal angular dependence of  $\exp(-il\phi)$ . This angular dependent phase allows the beam to carry angular momentum in the direction of propagation [8]. Note that, for  $l = 0$  we have a plane wave. At the atomic scale, we may say that [8]

$$\mathbf{J} = \mathbf{L} + \mathbf{S}, \tag{2}$$

whit  $\mathbf{J}$  the total angular momentum,  $\mathbf{L}$  and  $\mathbf{S}$  the

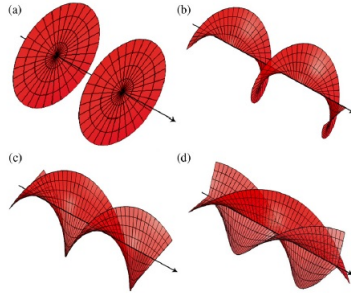


Figure 1: Helical phase fronts for  $l = 0$  in a),  $l = 1$  in b),  $l = 2$  in c) and  $l = 3$  in d) [10].

orbital and spin contributions for the angular momentum, respectively.

The momentum density per unit power of a (LG) mode (equation 1) is given by [8]

$$\mathcal{P} = \frac{|u|^2}{c} \left( \frac{rz}{(z^2 + z_R^2)} \mathbf{r} + \frac{1}{kr} \boldsymbol{\phi} + \mathbf{z} \right). \tag{3}$$

With some calculations, we can conclude that that

$$\frac{j_z}{\mathcal{P}_z} = \frac{J_z}{p_z c} = \frac{l}{\omega}. \tag{4}$$

Notice that we just consider the case with  $\mathbf{S} = 0$ . Nevertheless the previous result can be generalized for non-zero spin photons.

OAM beams can be generated through refractive or diffractive elements such as spiral phase plates, Dove prisms, meta-materials or Spatial Light Modulators (SLM) and Computer Generated Holograms (CGH). In the context of this work, we will focus on SLMs and CGHs. All these techniques offer great control and precision to imprint phase variations on the incident light to produce the OAM-carrying beams.

Although in a recent stage with some challenges to be overcome, many demonstrations have shown OAM potential to increase the spectral efficiency of today's communications due to the orthogonal relation between OAM states with (a lot) of different number of  $l$  modes. Used along with different multiplexing techniques, OAM may bring the new paradigm of optical communications. Moreover, OAM has applications in other fields, namely quantum information and quantum cryptography. Experimental and theoretical work showed that OAM may be a solution to the challenges found in these fields.

## 2 Computational Resources and Simulations

To generate OAM-carrying beams, two kinds of CGH can be used: spiral CGH and forked CGH. The former is displayed in figure 2. It is a linearised approximation to a more precise phase pattern and consists in the interference of a certain LG mode with a Gaussian mode. This approximation is not only simpler to implement but also sufficient for most applications [12, 13]. The forked CGH is the sum of a helical phase mask, which defines the beam topological charge, with a linear phase ramp. The role of the linear phase ramp is to spatially separate the phase-modulated beam from the zeroth-order non-phase-modulated beam. This means that if this kind of pattern is used, we will have to deal with the first diffraction order of the beam and discard the zeroth order, since the latter continues to be a Gaussian beam and the former is the one which carries the desired topological charge. Loading these phase patterns, or masks, onto the SLM through a computer, and aligning the beam with the CGH center, it is possible to imprint the desired topological charge on the incident beam. The topological charge imprinted onto the beam is the same as the one used for the mask [14]. If the mask's gray scale is inverted an OAM-carrying beam with a symmetric topological charge is produced.

A simple simulation of the beam's propagation and diffraction through some components was made as a control method to the experiment. To do it, the Angular Spectrum propagation method was implemented together with the Fresnel approximation, due to the complexity of the former method.

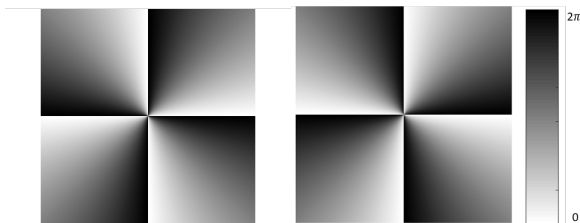


Figure 2: Spiral phase masks with topological charge  $l = 4$  (on the left) and  $l = -4$  on the right.

The Fresnel approximation can be expressed as [15]

$$\begin{aligned} U(x_0, y_0) &= \iint_{-\infty}^{\infty} U(x_1, y_1) \cdot h(x_0 - x_1, y_0 - y_1) dx_1 dy_1 \\ &= U(x_1, y_1) * h(x_1, y_1) \\ h(x_1, y_1) &= \frac{\exp(ikz)}{i\lambda z} \exp\left[\frac{ik}{2z}(x_1^2 + y_1^2)\right] \end{aligned} \quad (5)$$

where  $U(x_1, y_1)$  is an initial optical,  $U(x_0, y_0)$  is the optical field at the observation plane,  $\lambda$  represents the wavelength,  $k$  the wave number and  $z$  is the distance in the perpendicular direction of the observation plane. Expression 5 can be interpreted as a convolution, and thus we can make the simplification shown in equation 6 which makes use of the Fourier convolution theorem. The transfer function  $H(f_X, f_Y)$  is obtained through the Fourier transform of the Fresnel Diffraction approximation impulse response  $h(x_1, y_1)$  ( $f_X$  and  $f_Y$  denominate the spatial frequencies).

$$\begin{aligned} U(x_0, y_0) &= \mathcal{F}^{-1}\{\mathcal{F}\{U(x_1, y_1)\} \cdot H(f_X, f_Y)\} \\ H(f_X, f_Y) &= \exp(ikz) \cdot \exp[-i\pi\lambda z(f_X^2 + f_Y^2)] \end{aligned} \quad (6)$$

The diffraction of OAM-carrying beams is calculated regarding the transmittances of the used objects, namely a lens and a pinhole. Knowing that if an object has a transmittance  $t(x, y)$  an optical field, after diffraction, is given by [15]

$$U_t(x, y, 0) = U_i(x, y, 0)t(x, y) \quad (7)$$

If we Fourier transform the above equation, the convolution theorem of Fourier analysis allow us to write

$$\tilde{U}_t(f_X, f_Y) = \tilde{U}(f_X, f_Y) * T(f_X, f_Y) \quad (8)$$

where  $T(f_X, f_Y)$  is the Fourier transform of  $t(x, y)$ . Thus, the "new" angular spectrum is a characteristic of the diffractive component. For the used transmittances for the simulations were

$$t(x, y)_{LENS} = \exp\left[\frac{i2\pi}{\lambda} \frac{(x^2 + y^2)}{2f}\right] \quad (9)$$

for the plano-convex lens with focal distance  $f = 400\text{mm}$  and

$$t(x, y)_{PH} = \begin{cases} 1 & \text{if } (x^2 + y^2) < 150 \\ 0 & \text{otherwise.} \end{cases} \quad (10)$$

for the  $\text{Ø}150$  mm pinhole [16].

## 2.1 Simulation results

When running the simulations, the parameters were chosen to match the experimental ones: wavelength  $\lambda = 545$  nm, initial propagation distance  $z = 200$  mm and a width for the starting field  $w_0 = 9$  mm (the SLM's active area width). We chose  $l = 4$  for the spiral CGH and  $l = 2$  to the forked CGH. We used a 400 mm focal length, thin plano-convex lens and a pinhole  $\varnothing 150 \mu\text{m}$ .

All the experimental measurements are shown here to verify the validity of the simulations and consist in a direct measure of intensity, since the TN-LCoS technology used by our SLM allows us to do so [17].

Figures 3 and 4 show the simulations' results for initial fields and the respective propagation. Figure 5 show the experimental results. The simulations regarding spiral phase CGH show clear and accurate results which agree with the experimental measurements. Simulations performed with forked CGH don't present clearly the modulated

zeroth and first diffraction orders. Moreover, the simulation predicted the first diffraction order much closer to the zeroth order but experiments showed that this is not the case. This may happen because it was assumed that all the diffraction angles were small which may not be true when the beam is reflected by the SLM. The evidence for this fact lies on the distance between the zeroth and first diffraction orders (right side of figure 5).

The results for diffraction simulations of OAM-carrying beams are presented in figures 6 and 7

The simulations results are in good agreement with the experimental measurements in both cases. In lens diffraction, a central cross can be seen inside the pupil which captures the beam. A cross at the center can be clearly seen in either experimental and simulation results. Note that the pattern at the center of this cross is the same as the one presented in figure 5 (left side), this time with a smaller radius. Notice that we should focus our attention at the center of figure 6 since it contains the singularity that plays the central role on beam modulation

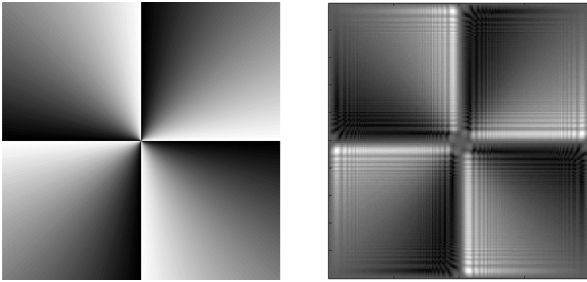


Figure 3: From left to right: Spiral CGH with topological charge  $l = 4$  (initial field); simulation of propagated field.

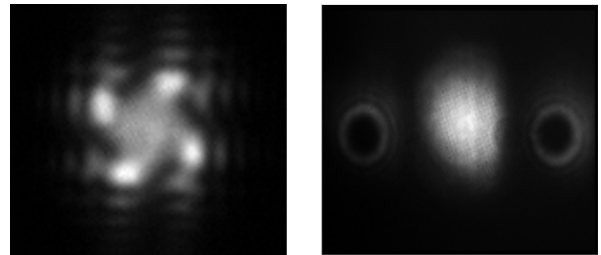


Figure 5: Experimental measurement: Spiral CGH with topological charge  $l = 4$  (left) and forked CGH with topological charge  $l = 2$  (right).

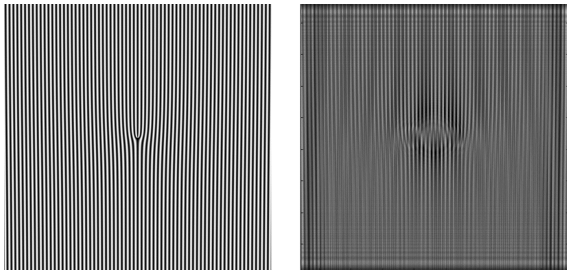


Figure 4: From left to right: Forked CGH with topological charge  $l = 2$  (initial field); simulation of propagated field.

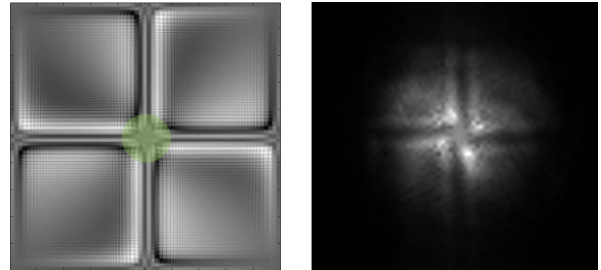


Figure 6: Simulation of a  $l = 4$  OAM carrying beam focused at the lens' focal plane. The green mark depicts the relevant simulation result.



Figure 7: Simulation of a  $l = 4$  OAM carrying beam diffracting through a  $150 \mu\text{m}$  pinhole.

(the region is depicted with a green spot).

### 3 Experimental Setup

#### 3.1 OAM (de)modulation

Although two different setups were required for each stage of the experiment, the setup described here is not totally independent from the one used for information transmission. Apart from performing a correct modulation and demodulation, this setup should also be enabled for performing information transmission without requiring a realignment. Due to this reason, the multiplexing of the beams is implemented from the beginning, although it is not related directly with the main goal of this stage.

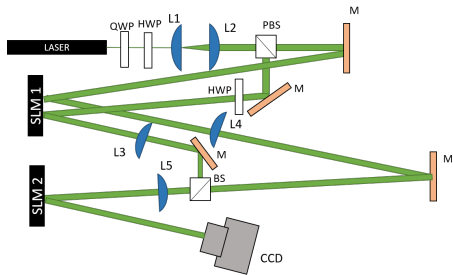


Figure 8: Schematic of the experimental setup: QWP- Quarter wave plate; HWP - Half wave plate; L1 and L2 - plano-convex lenses with  $f = 35\text{mm}$  and  $f = 35\text{mm}$ , respectively; PBS - Polarizing beamsplitter; L3 to L5 - plano-convex lenses with  $f = 250\text{mm}$ ; BS- Beamsplitter; M-Mirror.

Figure 8 shows a schematic of the implemented setup. A  $545 \text{ nm}$  HeNe laser with a beam width of

$\sim 1\text{mm}$  and an average divergence of  $0.647 \text{ mrad}$  was used. Although the manufacturer announces a linearly polarised laser, during its characterization it was found that a circular component was present and thus, since the SLM's efficiency is higher when linear polarization is used, a Quarter Wave Plate (QWP) was used to minimize the circular components. Also, an Half Wave Plate (HWP) was used after the QWP to control the polarization direction of the beam. A beam expander with  $35 \text{ mm}$  and  $75 \text{ mm}$  lenses was set so that the beam width is increased to  $\sim 2 \text{ mm}$ . This set of lenses was not chosen by chance: it is convenient that the beam is large enough to ensure the quality of the modulation but, at the same time, the beam can't be very wide, since we will be modulating two beams in the same SLM and after modulation the beam diameter increases (equation 11 [18]).

$$d_{LG}(I_{max}) = \sqrt{\frac{|l|}{2}}w(z) \quad (11)$$

The original beam is then split by a PBS into two beams to be modulated in different ways. Two mirrors were placed to reflect each beam to the SLM, minimizing the angle of incidence in this component (small angles of incidence improve the modulation [19, 20]). Another HWP was placed in the reflected beam's path to rotate its polarization  $90^\circ$ . This was done because this beam's polarization was mainly vertical and, during the experiment, it was concluded that horizontally polarized light optimized the wavefront phase modulation, while a lot of noise was founded if vertical polarization was maintained. Also, in this step of the alignment, we needed to be careful with both beams' positions inside the SLM's active area. Not only these had to be well separated from each other, in order to avoid interference, but neither is it convenient to be close to SLM' active area's edges, because it could compromise the modulation quality. After this, the beams are multiplexed with a BS and reflected by a mirror to the second SLM so that one of them is demodulated. To choose the beam to demodulate, we load into the SLM the inverse mask used in its modulation. In order to check that these two processes were done correctly the beams are captured individually with a CCD-WFS (Phasics model SID4). Note that, for alignment purposes, each beam is modulated individually and not simultaneously. To verify and optimize the modulation process for one

beam, the other is blocked in order not to interfere while being captured. Only when a transmission of information occurs, is the SLM 1 used to modulate both beams at the same time.

We shall now justify the use of a 4f lens system in our set up. It is known that the width of a LG beam is given by 11 [18] and that its divergence increases with  $|l|$ . This divergence, even in small distances, makes the alignment of the demodulation process very difficult [21]. To minimize the effects of that divergence, we used 2 lenses of 250 mm focal length for each beam so that we could have an image of the modulated beam near the second SLM.

### 3.2 (De)Multiplexing and transmission of information

As already mentioned, this experimental setup is based on the previous one. Figures 9 show a schematic of the implemented setup to perform transmission of information. The beam multiplexing is performed with the BS. The beam demultiplexing is performed by means of spatial filtering [13]. To be demultiplexed, both beams are focused by a 400 mm lens and pass through a 150  $\mu\text{m}$  pinhole, where the back-converted Gaussian beam is separated from the OAM-carrying beam. The pinhole size was chosen by making some calculations based on equation 12 [22, 23] where  $f$  rep-

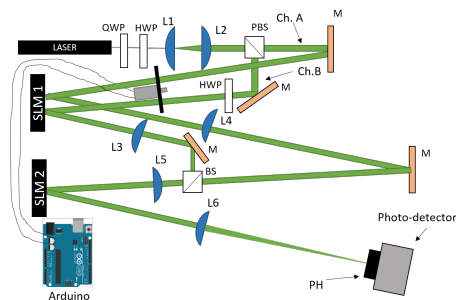


Figure 9: Schematic of the experimental setup: QWP- Quarter wave plate; HWP - Half wave plate; L1 and L2 - plano-convex lenses with  $f = 35\text{mm}$  and  $f = 35\text{mm}$ , respectively; L3 to L5 - plano-convex lenses with  $f = 250\text{mm}$ ; L6 - plano-convex lenses with  $f = 400\text{mm}$ ; PBS - Polarizing beam-splitter; BS- Beamsplitter; M-Mirror; PH - Pinhole ( $\text{Ø}150\text{mm}$ ).

resents the lens focal distance,  $\lambda$  the beam wavelength,  $w_0$  its focused waist size and  $D$  the beam diameter at the lens plane. The used pinhole is slightly larger than  $2w_0$ , as recommended, to avoid diffraction rings and loss of power [23].

$$\text{Beam Spot Size} = 2w_0 = \frac{4f\lambda}{\pi D} \quad (12)$$

After this, the light intensity is measured with a photodetector (Thorlabs model DET10A) connected through a coaxial cable to a digital oscilloscope (Picoscope 3200). Finally, the information encoding is performed with an On/Off Keying (OOK) system implemented by a circular chopper fixed in a Servo motor controlled by an Arduino board. The chopper has two concentric rings of holes, each one assigned to a beam: the inner ring encodes 45 information bits into the beam transmitted in the first PBS, and the outer ring encodes 60 bits into the beam reflected in the same PBS. Since we use two different channels of information, it is simpler to denominate the transmitted and reflected beams described above by channel A and channel B, respectively.

## 4 Results

### 4.1 Modulation and back conversion

Three different topological charges were used to modulate the beams in each channel. Channel A was modulated with topological charges of  $l = -4, 2, 4$ , and channel B with  $l = 4, 6$  (each modulation is performed in distinct information transmissions). To do this, the masks with inverse topological charge are loaded in SLM 1 while SLM 2 is turned off. It should be said that forked CGH were tested but the obtained results were poor. Moreover, the fact that the first order diffraction is needed made the alignment and measurement harder. Given these reasons, forked CGH were abandoned and all the results were obtained with spiral CGH.

#### 4.1.1 Spiral phase CGH for modulation

Three transmissions of information were performed. In each transmission a different combination of topological charges was used. The OAM beams with positive topological charges used in the

first transmission are shown in figures 10 and 11. In the second transmission, symmetric topologi-

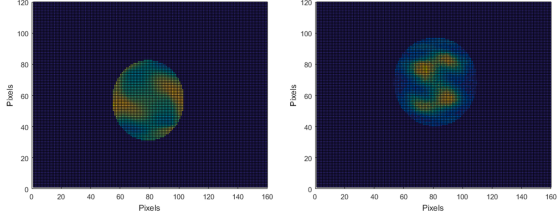


Figure 10: From left to right: normalized phase profile for  $l = 2$  OAM beam; normalized intensity profile for the same beam ( $l = -2$  spiral phase mask loaded on SLM 1 with SLM 2 turned off). These results refer to channel A.

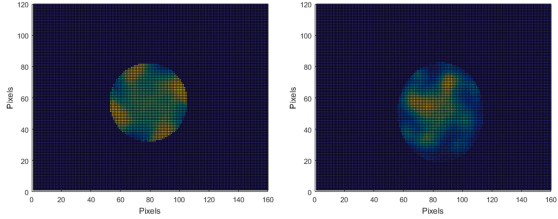


Figure 11: From left to right: normalized phase profile for  $l = 4$  OAM beam; normalized intensity profile for the same beam ( $l = -4$  spiral phase mask loaded on SLM 1 with SLM 2 turned off). These results refer to channel B.

cal charges were used with  $|l| = 4$ . The phase and intensity modulations achieved for channel A are shown in figure 12. The phase and intensity profiles for channel B are already presented above on figure 11. Note that channel A, once carrying a topological charge of opposite sign but same absolute value of that of channel B, results in the same number of peaks in intensity with a vortex spinning in the opposite direction. This confirms the physical interpretation of the sign of  $l$  and ensures that the modulation has been performed as expected. For the third transmission, channel A was imprinted with the symmetrical OAM ( $l = 4$ ) while channel B was imprinted with a  $l = 6$  topological charge. The phase and intensity profiles for both channels are presented in figures 13 and 14. In general, the phase modulation is satisfactory for all topological charges in both channels since the number of peaks

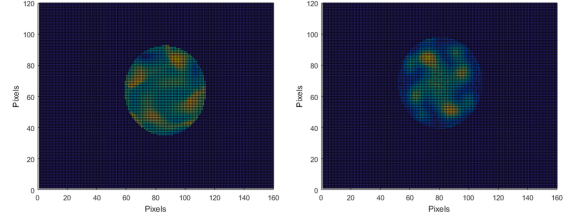


Figure 12: From left to right: normalized phase profile for  $l = -4$  OAM beam; normalized intensity profile for the same beam ( $l = 4$  spiral phase mask loaded on SLM 1 with SLM 2 turned off). These results refer to channel A.

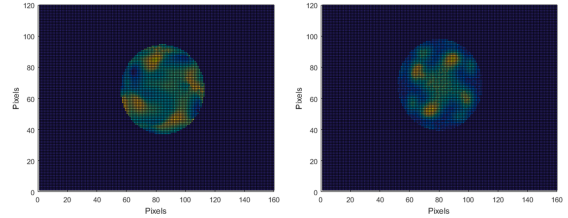


Figure 13: From left to right: normalized phase profile for  $l = 4$  OAM beam; normalized intensity profile for the same beam ( $l = -4$  spiral phase mask loaded onto SLM 1 with SLM 2 turned off). These results refer to channel A.

and respective variations to the minima correspond with the expected results, just as predicted by the simulations described in section 2. Regarding the intensity, a more detailed analysis is needed. The results are also good since the amplitude-phase coupling makes the intensity follow the same pattern as the phase. Moreover, the vortex spinning directions can be clearly observed and match the expected rotation direction. It is known that theoretically, an intensity singularity is expected at the wavefront sensor. Accounting the modulations on channel A, even though the intensity is not zero at the center, it distinctly has a lower value. For channel B the case is not so clear. Although the intensity peaks are well defined, there is an excess at the center. This fact can be explained taking into account that the light polarization for this mode has to be adjusted with a HWP (see chapter 3). Although efforts were made to reduce the polarization circular components which come from the laser and to optimize the direction of channel B, the modulation

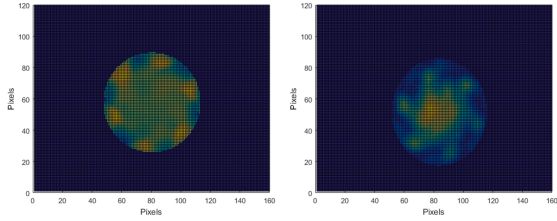


Figure 14: From left to right: normalized phase profile for  $l = 6$  OAM beam; normalized intensity profile for the same beam ( $l = -6$  spiral phase mask loaded onto SLM 1 with SLM 2 turned off). These results refer to channel B.

quality is not as great as that of channel A.

## 4.2 Back-conversion of OAM modes

To perform the demodulation process, SLM 2 must be loaded with the inverse mask used in SLM 1 to modulate the respective channel. It is expected, ideally, that the back converted mode has no OAM, thus presenting a Gaussian intensity shape together with the phase of a plane wave. To demodulate the beam of channel A with the topological charge used in the first transmission, an  $l = 2$  mask was loaded in SLM 2, resulting in the demodulation presented in figure 15. For channel B, the same was done with an  $l = 4$  mask, obtaining the results shown in figure 16. Figure 17 presents the back conversion of the modulated beam used in channel A in the second transmission (the demodulation for channel B is the same presented in figure 16). Figures 18

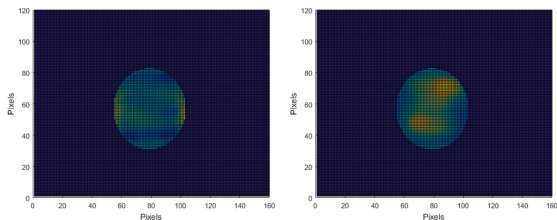


Figure 15: From left to right: normalized phase profile for the back conversion of an  $l = 2$  OAM beam; normalized intensity profile for the same back converted beam ( $l = -2$  spiral phase mask loaded on SLM 1 and  $l = 2$  loaded on SLM 2 ). These results refer to channel A.

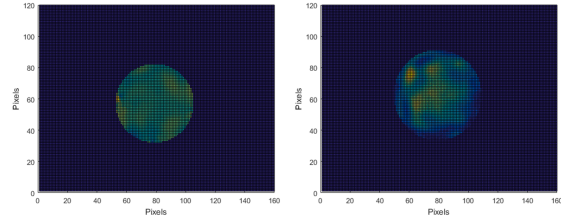


Figure 16: From left to right: normalized phase profile for the back conversion of an  $l = 4$  OAM beam; normalized intensity profile for the same back converted beam ( $l = -4$  spiral phase mask loaded on SLM 1 and  $l = 4$  loaded on SLM 2 ). These results refer to channel B.

and 19 do the same with the profiles obtained for the back conversion of channels A and B in the third transmission.

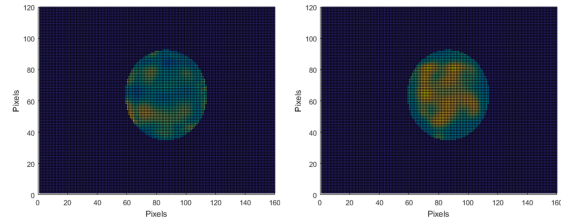


Figure 17: From left to right: normalized phase profile for the back conversion of an  $l = -4$  OAM beam; normalized intensity profile for the same back converted beam ( $l = 4$  spiral phase mask loaded on SLM 1 and  $l = -4$  loaded on SLM 2 ). These results refer to channel A.

Once more the results regarding phase are, in general, satisfactory. The back converted phase profiles resemble the phase of a plane wave with smooth variations. These variations are experimentally expected since they may arise from misaligned optical components or some parts of the wavefront that were not properly demodulated. Observing intensity, the results are unclear. In some cases (figures 15 and 17) the intensity peaks are still observable although their intensity is attenuated and more distributed over the wavefront. Other results don't show well shaped peaks but the intensity profile is not Gaussian either. Due to the limitations of the used SLM, the random modulation generated by the SLM pixel matrix may be responsible

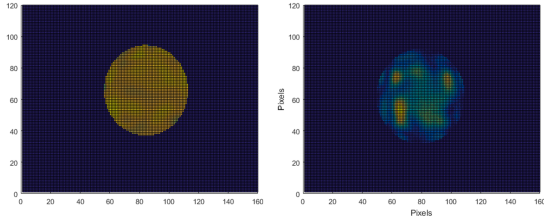


Figure 18: From left to right: normalized phase profile for the back conversion of an  $l = 4$  OAM beam; normalized intensity profile for the same back converted beam ( $l = -4$  spiral phase mask loaded on SLM 1 and  $l = 4$  loaded onto SLM 2 ). These results refer to channel A.

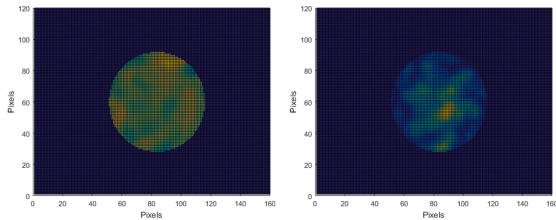


Figure 19: From left to right: normalized phase profile for the back conversion of an  $l = 6$  OAM beam; normalized intensity profile for the same back converted beam ( $l = -6$  spiral phase mask loaded on SLM 1 and  $l = 6$  loaded on SLM 2 ). These results refer to channel B.

for these effects. Furthermore, the amplitude-phase coupling effect also prevent the intensity from acquiring a Gaussian shape. These facts makes the goal of achieving an intensity profile close to the expected very difficult, if not impossible. Despite the (de)modulation imperfections, the information transmissions were executed and provided satisfactory results.

### 4.3 Transmission analysis

As stated before, the first transmission was executed using a beam with topological charge  $l = 2$  for channel A and topological charge  $l = 4$  for channel B (figures 10 and 11 show the modulated phase and intensity profiles for each channel). The bit error rates (BERs) calculated for each channel are present in table 1. At first sight, the obtained BER may seem to be high when compared to those from

other state-of-the-art works [12, 13, 24, 25, 26]. Nevertheless, we should notice that, due to the bit-streams small length, the lowest BER that may be find for channels A and B are, respectively  $\frac{1}{45} \simeq 0.022$  and  $\frac{1}{60} \simeq 0.017$  and so the obtained values (apart from the 21% BER obtained for channel B in the first transmission) are actually good, indicating that the experimental apparatus is working properly. Despite the above argument, the very high BER presented by channel B are not satisfactory even for a proof of concept experiment. This raised the suspicion that maybe the demultiplexing process for channel A was not being done correctly, due to the small size of the beam. To check this possibility, we changed the topological charge of channel A, replacing the used mask with another of topological charge  $l = -4$ . This way, both channels use beams with the same topological charge (in absolute value), leaving no space for issues related with beam size. The second transmission was performed in these conditions. The BER can be seen in table 1.

Topological charge		BER	
Ch. A	Ch. B	Ch. A	Ch. B
2	4	0.067	0.217
-4	4	0.067	0.067
-4	6	0.022	0.050

Table 1: BER for channels A and B modulated with different topological charges.

The results confirm the suspicion, since the BER for channel B has decreased one order of magnitude. To test the hypothesis that the demultiplexing process efficiency can be improved by increasing the topological charge in absolute value, a third transmission was performed leaving the absolute value of channel's A topological charge untouched and changing the one of channel B to  $l = 6$ . As the values of table 1 show, the above hypothesis is confirmed. Note that when the topological charge of a channel is increased (in absolute value), the BER of the neighbour channel decreases. This happens because the beam size increases with  $|l|$ , which means that when the beam passes through the pinhole, more intensity is left behind and less power is detected from that channel. This means that there is less power to be leaked in the channel that is

Channel A			
Top. charge	No CT	Atten. CT	w/ CT
-4	0	0	0.067
2	0	0.044	0.067
4	0	0	0.022

Table 2: BER values for different levels of crosstalk (CT) obtained for channel B.

Channel B			
Topological charge	No CT	Atten. CT	w/ CT
4 (Ch. A $l = 2$ )	0	0.050	0.217
4 (Ch. A $l = -4$ )	0	0.017	0.067
6	0	0	0.05

Table 3: BER values for different levels of crosstalk (CT) obtained for channel B.

being detected and thus lower BER are achieved. The most probable cause for the remaining wrongly detected bits, as the previous result suggest, is concerned with power dissipated from one channel to another, in other words, there is crosstalk causing a wrong bit detection. To evaluate this, the second and third transmissions were repeated twice in different conditions: in the first time the channel which was not being measured was completely blocked; in the second time the same was done but the non-captured channel was only partially blocked (the intensity was roughly reduced to half). As expected, the results presented in tables 2 and 3 show that there are no errors when there is no crosstalk and BER increase when the intensity of the neighbour channel also increases.

Such crosstalk levels mean that the demultiplexing process should be more efficient. This is probably related with the back-conversion of OAM modes. Since the used photo-detector detects the intensity, imperfections in the demodulation depicted in the previous section may be a source of error.

## 5 Conclusions

We started by simulating the propagation and diffraction of OAM modes generated with two different types of masks: spiral and forked phase pat-

terns.

After that, we have implemented an experimental setup that is able to perform beam modulation and demodulation so that OAM-carrying beams may be generated. The setup is also prepared to perform transmissions of information using two channels encoded with distinct bitstreams. Full polarization control was needed to achieve better modulations and demodulations of the beams' wavefronts. After the completion of this work, the following conclusions can be stated:

forked CGH don't provide a good phase modulation. Moreover, the fact that the first order diffraction of the reflected beam must be used makes the alignment and measurement harder; this setup was sensitive to polarization since TN-LCoS technology was used; the effects of polarization can be reduced if the beam is polarized in the direction which maximizes the SLM performance; the OAM modes' detected power decreases if  $|l|$  is increased; the demultiplexing process although effective could be more efficient. This is probably due to the imperfections from the OAM modes back conversion; OAM is a property of light that can be used to multiplex information and thus be used in optical communications to increase the communications' capacity and spectral efficiency.

This proves that our setup although simple and modest is robust and could achieve the main goals for this work.

### 5.1 Future Work

The first change to improve the experiment would be the implementation of a polarization insensitive mechanism as shown in the work done by Hu *et al.* [27]. This would allow to perform a better modulation and avoid the intensity peaks observed at the center of the wavefront as well as to spot other noise sources. The use of longer bit streams would provide more solid conclusions on BER as well as the use of a lock-in amplifier would enhance the transmission performance.

Additional objectives can be stated to future experiments in order to implement features that are present in any actual communication network. Since information transmission was achieved, the next step may be the implementation of more channels and perform the multiplexing process using OAM together with other already established

methods. Finally, the implementation of data exchange would be another important achievement, since it is a key process in nowadays communication networks[28, 29].

## References

- [1] Takeshi Kmiya, Tetsuya Miyazaki, and Fumito Kubota. Social Demand of New Generation Information Network: Introduction to High Spectral Density Optical Communication Technology. 2010.
- [2] C.E: Shannon. A Mathematical Theory of Communication\*. *Mobile Computing and Communications Review*, 5(1), 2001.
- [3] Gordon Moore. Cramming More Components onto Integrated Circuits. *Proceedings of the IEEE*, 86, 1998.
- [4] Yurii Vlasov. Silicon photonics for next generation computing systems. European Conference on Optical Communications, 2008.
- [5] Prachi Sharma, Suraj Pardeshi, Rohit Kumar Arora, and Mandeep Singh. A Review of the Development in the Field of Fiber Optic Communication Systems. *International Journal of Emerging Technology and Advanced Engineering*, 2013.
- [6] Peter Winzer. Modulation and multiplexing in optical communication systems. *Research Highlights*, 2009.
- [7] A. E. Willner, H. Huang, Y. Yan, N. Ahmed, G. Xie, C. Bao, L. Li, Y. Cao, Z. Zhao, J. Wang, M. P. J. Lavery, M. Tur, S. Ramachandran, A. F. Molisch, N. Ashrafi, and S. Ashrafi. Optical communications using orbital angular momentum beams. *Advances in Optics and Photonics*, 7, 2015.
- [8] L. Allen, M. W. Beijersbergen, R. J. C. Spreeuw, and J. P. Woerdman. Orbital Angular Momentum of light and the transformation of Laguerre-Gaussian laser modes. *Physical Review*, A(45), 1992.
- [9] Miles Padgett, Johannes Courtial, and Les Allen. Light's orbital angular momentum. *Physics Today*, 57(5):35–40, 2004.
- [10] Alison M. Yao and Miles J. Padgett. Orbital angular momentum: origins, behavior and applications. *Advances in Optics and Photonics*, 3:161–204, 2011.
- [11] Johan Sjöholm and Kristoffer Palmer. *Angular Momentum of Electromagnetic Radiation*. Faculdade de Ciências - Universidade de Uppsala, 2007.
- [12] Nenad Bozinovic, Yang Yue, Yongxiong Ren, Moshe Tur, Poul Kristensen, Hao Huang, Alan Willner, and Siddharth Ramachandran. Terabit-Scale Orbital Angular Momentum Mode Division Multiplexing in Fibers. *Science, AAAS*, 2013.
- [13] Jian Wang, Jeng-Yuan Yang, Irfan M Fazal, Nisar Ahmed, Yan Yan, Hao Huang, Yongxiong Ren, Yang Yue, Samuel Dolinar, Moshe Tur, et al. Terabit free-space data transmission employing orbital angular momentum multiplexing. *Nature Photonics*, 6(7):488–496, 2012.
- [14] Ting-Chung Poon and Jung-Ping Liu. *Introduction to Modern Digital Holography with MATLAB*. Cambridge University Press, 2014.
- [15] Joseph W Goodman. *Introduction to Fourier optics*. Roberts and Company Publishers, 2005.
- [16] B. E. A. Saleh and M. C. Teich. *Fundamentals of photonics*. Wiley series in pure and applied optics. Wiley, 2nd edition, 2007.
- [17] Andrés Márquez Ruiz. *Accurate predictive model for twisted nematic liquid crystal devices. Application for generating programmable apodizers and Fresnel lenses*. PhD thesis, Universitat Autònoma de Barcelona, Bellaterra, June 2001.
- [18] Miles J Padgett, Filippo M Miatto, Martin PJ Lavery, Anton Zeilinger, and Robert W Boyd. Divergence of an orbital-angular-momentum-carrying beam upon propagation. *New Journal of Physics*, 17(2):023011, 2015.
- [19] A Lizana, N Martín, M Estapé, E Fernández, I Moreno, A Márquez, C Iemmi, J Campos, and MJ Yzuel. Influence of the incident angle in the performance of liquid crystal on silicon displays. *Optics express*, 17(10):8491–8505, 2009.

- [20] Walter Harm, Clemens Roider, Stefan Bernet, and Monika Ritsch-Martel. Tilt-effect of holograms and images displayed on a spatial light modulator. *Optics express*, 23(23):30497–30511, 2015.
- [21] Shilie Zheng, Xiaonan Hui, Jiangbo Zhu, Hao Chi, Xiaofeng Jin, Siyuan Yu, and Xianmin Zhang. Orbital angular momentum mode-demultiplexing scheme with partial angular receiving aperture. *Optics express*, 23(9):12251–12257, 2015.
- [22] Understanding Spatial Filters. Visited on August 2016.
- [23] Spatial Filters. Visited on August 2016.
- [24] Hao Huang, Guodong Xie, Yan Yan, Nisar Ahmed, Yongxiong Ren, Yang Yue, Dvora Rogawski, Moshe J Willner, Baris I Erkmen, Kevin M Birnbaum, et al. 100 tbit/s free-space data link enabled by three-dimensional multiplexing of orbital angular momentum, polarization, and wavelength. *Optics letters*, 39(2):197–200, 2014.
- [25] Miles Padgett, Hao Huang, Yongxiong Ren, and Giuseppe Caire. Experimental demonstration of 16 Gbit/s millimeter-wave communications using MIMO processing of 2 OAM modes on each of two transmitter/receiver antenna apertures. *Global Communications Conference (GLOBECOM)*, IEEE, 2015.
- [26] Jian Wang, Shuhui Li, Ming Luo, Jun Liu, Chao Li, Dequan Xie, Qi Yang, Shaohua Yu, Junqiang Sun, Xinliang Zhang, William Shieh, and Alan Willner. N-Dimensional Multiplexing Link with 1.036-Pbit/s Transmission Capacity and 112.6-bit/s/Hz Spectral Efficiency using OFDM-8qam Signals over 368 WDM Pol-Muxed 26 OAM Modes. *European Conference of Optical Communications (ECOC)*, 2014.
- [27] L. Hu, X. Li, Q. Mu, Z. Cao, D. Li, Y. Liu, Z. Peng, and X. Lu. A polarization independent liquid crystal adaptive optics system. *Journal of Optics*, 12, 2010.
- [28] Jian Wang and Alan E. Willner. Optical Signal Processing: Data Exchange. In *Design and Architectures for Digital Signal Processing*. In-Tech, 2013.
- [29] Yang Yue, Nisar Ahmed, Hao Huang, Yan Yan, Yongxiong Ren, Dvora Rogawski, and Alan E Willner. Reconfigurable orbital-angular-momentum-based switching among multiple 100-gbit/s data channels. In *Optical Fiber Communication Conference*, pages OM2G–1. Journal of Optical Society of America, 2013.